New Templated Ostwald Ripening Process of Mesostructured FeOOH for Third-Harmonic Generation Bioimaging

Chien-Wei Lee, Pei-Chun Wu, I-Ling Hsu, Tzu-Ming Liu,* Wai-How Chong, Cheng-Ham Wu, Tsung-Yuan Hsieh, Lun-Zhang Guo, Yu Tsao, Po-Ting Wu, Jiashing Yu, Pei-Jane Tsai, Huei-Sheng Huang, Yu-Chun Chuang, and Chih-Chia Huang*

Emerging advances in iron oxide nanoparticles exploit their high magnetization for various applications, such as bioseparation, hyperthermia, and magnetic resonance imaging. In contrast to their excellent magnetic performance, the harmonic generation and luminescence properties of iron oxide nanoparticles have not been thoroughly explored, thus limiting their development as a tool in photomedicine. In this work, a seed/growth-inspired synthesis is developed combined with primary mineralization and a ligand-assisted secondary growth strategy to prepare mesostructured α-FeOOH nanorods (NRs). The sub-wavelength heterogeneity of the refractive index leads to enhanced third-harmonic generation (THG) signals under near-infrared excited wavelengths at 1230 nm. The as-prepared NRs exhibit an 11-fold stronger THG intensity compared to bare α-FeOOH NRs. Using these unique nonlinear optical properties, it is demonstrated that mesostructured α-FeOOH NRs can serve as biocompatible and nonbleaching contrast agents in THG microscopy for long-term labeling of cells as well as in angiography in vivo by modifying lectin to enhance the binding efficiency to the glycocalyx layers on the wall of blood vessels. These results provide a new insight into Fe-based nanoplatforms capable of emitting coherent light as molecular probes in optical microscopy, thus establishing a complementary microscopic imaging method for macroscopic magnetic imaging systems.

1. Introduction

The material α-FeOOH (goethite), one of the ferric oxyhydroxide (FeOOH) polymorphs, has been widely used in industrial applications as pigments,[1] electrodes,[2–4] sorbents,[5–7] and precursors of powders for magnetic applications.[8] Additionally, FeOOH particles are the most important starting materials in the synthesis of iron oxides such as hematite (α-Fe$_2$O$_3$) and maghemite (γ-Fe$_2$O$_3$) for applications as semiconductors and magnetic contrast agents.[9] Apart from these uses in industrial, energy, and magnetic fields, few optical investigations have studied several distinct kinds of iron oxide nanomaterials, thus limiting the development of these materials as optical sensors, for microscopic imaging, and in photon-to-thermal therapy in photomedicine.[10,11] Recently, our group[12,13] and other researchers[14,15] reported that surface-modified and/ or highly crystalline Fe$_3$O$_4$ nanoparticles exhibited strong near-infrared (NIR)

C.-W. Lee, Dr. I.-L. Hsu, Prof. C.-C. Huang
Department of Photonics, Center of Applied Nanomedicine, Center
for Micro/Nano Science and Technology and Advanced Optoelectronic
Technology Center
National Cheng Kung University
Tainan 70101, Taiwan
E-mail: c2huang@mail.ncku.edu.tw
Dr. P.-C. Wu, Prof. T.-M. Liu, W.-H. Chong
Institute of Translational Medicine
Faculty of Health Sciences
University of Macau
Macao SAR 999078, China
E-mail: tmliu@umac.mo
Dr. C.-H. Wu, T.-Y. Hsieh, L.-Z. Guo
Institute of Biomedical Engineering & Molecular Imaging Center
National Taiwan University
Taipei 10617, Taiwan

Dr. Y. Tsao
Research Center for Information Technology Innovation
Academia Sinica
Taipei 11529, Taiwan
P.-T. Wu, Prof. J. Yu
Department of Chemical Engineering
National Taiwan University
Taipei 10617, Taiwan
Prof. P.-J. Tsai, Prof. H.-S. Huang
Department of Medical Laboratory Science and Biotechnology
College of Medicine
National Cheng Kung University
Tainan 70101, Taiwan
Dr. Y.-C. Chuang
National Synchrotron Radiation Research Center
Hsinchu 300, Taiwan

ADVANCED
SCIENCE NEWS

www.advancedsciencenews.com

NANO · MICRO
small
www.small-journal.com

absorption for efficient NIR-to-thermal ablation of cancerous cells at a low power within 10 min of irradiation. These unique NIR absorption properties of iron oxide–based nanomaterials were recently used in applications as fluorescent probes,[16] polymerase chain reaction (PCR) photoheaters,[17] and repeatable photothermal scaffolds.[18]

Despite the success of magnetic and optical dual functions of inverse spinel-structured iron oxides (i.e., γ-Fe$_2$O$_3$ and Fe$_3$O$_4$), antiferromagnetic α-FeOOH nanomaterials are failed to achieve high magnetization, resulting in their poor suitability for magnetic applications. The low magnetization features of α-FeOOH nanocrystals are difficult to improve and overcome. Rather than a magnetic function, the high refractive index of FeOOH ($n = 2.327$)[19] has the potential to generate strong optical contrast with third-harmonic generation (THG). According to the nonlinear optical theory of focused Gaussian beams,[20] the THG yield is sensitive to the difference in the refractive index within the focal volume. This contrast mechanism has been demonstrated on silicon nanowires in vivo with high imaging resolution.[21] In contrast to the toxic Cd-based quantum dots (QDs),[22] FeOOH nanoparticles showed improved biocompatibility as the contrast agent. The development of nonbleachable THG contrast from biocompatible nanoparticles at NIR II excitation wavelength would be a valuable contrast agent for long-term labeling and cell tracking, but was rarely discussed.[23,24] Until recently, Dubreil et al. demonstrated that bismuth ferrite harmonic nanoparticle-labeled stem cells were successfully visualized at a depth of more than 1.3 mm from the tissue surface. This observation was made possible by an 1300 nm excitation laser with a pulse-width shorter than 120 fs.[24] This excitation at NIR II wavelength (1100–1350 nm) has superior tissue transmission than that at the NIR I wavelengths due to the reduction in scattering attenuation and the autofluorescence from tissues.[23]

In this report, shape- and size-controllable synthesis of FeOOH mesostructures was developed on the basis of a new methodological concept of primary mineralization to form colloidal templates followed by a ligand-assisted secondary growth strategy. The uniformity and size focusing of the FeOOH mesostructures were obtained owing to the Ostwald ripening mechanism to tailor the structure of the endogenous FeOOH particle. This second growth of iron species at the surface of the primary FeOOH particle was different from the conventional dissolution and re-precipitation reaction of fresh solute in the continuous-phase solution.[25] Excited by a 1230 nm (NIR II) femtosecond laser, the α-FeOOH rod-like mesostructures can generate 11-fold stronger THG contrast because of enhanced absorption. In contrast to other single-photon contrast agents,[10,11,26] the developed α-FeOOH rod-like mesostructures have low cytotoxicity and exhibit nonbleaching THG signals suitable for long-term cell imaging or the study of particle metabolism by cells. This α-FeOOH rod-like mesostructure was further functionalized with polydopamine and lectin[27–29] to enhance the binding affinity of α-FeOOH rod-like mesostructures to the glycocalyx layers on the wall of blood vessels. This design achieves the in vivo labeling of vessel walls in THG microscopy. Further conjugation with QDs enables two-photon fluorescence and THG dual contrasts, which is a potential development for imaging studies on the co-release of drug-immobilized QDs from hybrid carriers.

2. Results and Discussion

Detailed synthetic procedures are provided in the Supporting Information. In brief, a 50×10^{-3} M FeCl$_2$ solution was prepared with deionized water and sealed for use on different days. After aging the FeCl$_2$ solution for 39 days to form bare iron oxide nanorods (NRs), 10 mL of the Fe-based mother solution was reacted with trimesic acid (TMA) and sodium citrate in a Teflon-lined stainless steel autoclave at 200 °C for 3 h. The crude product was then purified through a centrifugation-washing process with deionized water for subsequent applications. **Figure 1**a (scanning electron microscopy (SEM)) and Figure 1b (transmission electron microscopy (TEM)) show the broad view of the rods, indicating possible mass production of uniform materials. Accordingly, an average length of ≈96 nm and an average width of ≈43 nm (aspect ratio of 2.23) were measured. The iron and oxygen compositions of the rod-like particles were also verified by energy-dispersive X-ray spectroscopy (EDS), as displayed in the right panel of Figure 1b. The bright-field and corresponding dark-field images in Figure 1c,d, respectively, show the homogenous atom distribution on a single FeOOH mesostructure without other impurity phases. The X-ray diffraction (XRD) patterns (Figure 1e) display all the diffraction peaks that can be indexed as orthorhombic α-FeOOH (space group: *Pbnm*, No. 62) with cell constants of $a = 4.610$ Å, $b = 9.956$ Å, and $c = 3.024$ Å, which are consistent with the reported data (JCPDS card 29–713). We further characterized the rod-like FeOOH mesostructures through high-resolution TEM (HR-TEM) in Figure 1f, which demonstrates the porous texture of the structures appearing on the surface of the FeOOH NRs. Fast Fourier transform (FFT) with a [001] zone axis was further performed and showed a single crystalline like pattern (Figure 1f$_1$). The lattice fringes in the HRTEM images of a [001]-oriented single rod-like FeOOH particle also show periods of $d_1 = 0.24$ nm, $d_2 = 0.27$ nm, and $d_3 = 0.23$ nm with respect to the (040), (130), and (200) planes. The (040) planes repeating along the long-axis further confirm that the longitudinal direction is the *b*-axis and that the perpendicular orientation to the ⟨010⟩ is the *a*-axis. Figure 1f$_2$ reveals the adhesion of secondary FeOOH seed particles, marked with white dotted lines, to the primary particles that were epitaxially grown along the [100] and/or [130] directions.

To validate the formation of mesostructures in relation to the secondary growth process, time-dependent TEM analysis was performed to monitor the hydrothermal reaction products from 0.5 to 2 h. We used an FeCl$_2$ solution aged for 30 days as an example. The results in Figure S1 in the Supporting Information show the TEM images of rod-like FeOOH nanocrystals with aspect ratios of 2.80 at 0.5 h (length: 57.8 nm and width: 20.6 nm) and 2.78 at 1 h (length: 60.6 nm and width: 21.8 nm). As the reaction proceeded to 1.5 h, several small nanocrystals grown on the surface of the crude FeOOH NRs were an average of 64.7 nm in length and 25.3 nm in width.
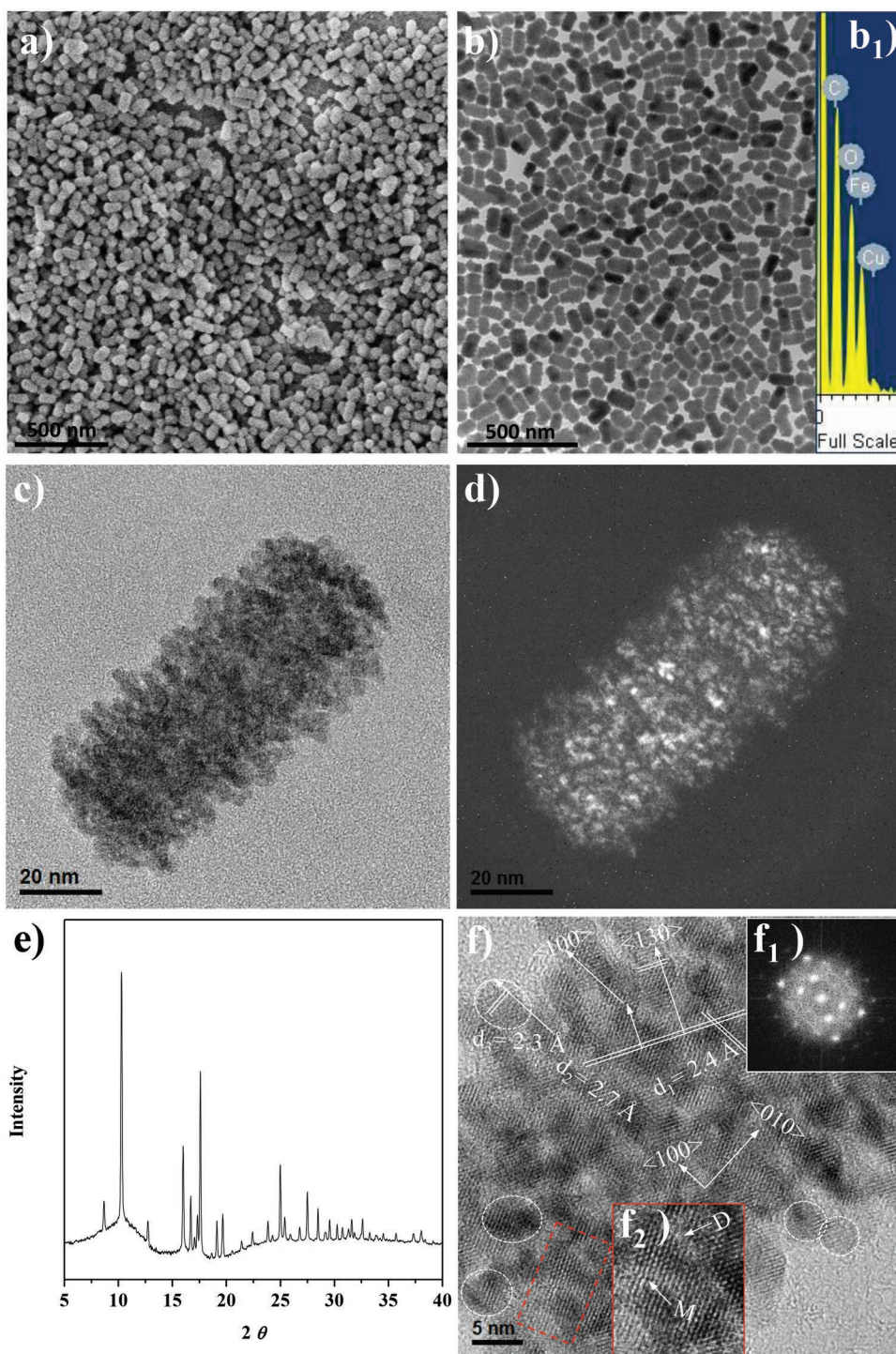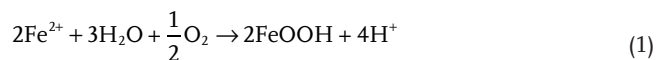
ADVANCED
SCIENCE NEWS
www.advancedsciencenews.com

NANO · MICRO
small
www.small-journal.com

Figure 1. a) SEM and b) TEM images and b$_1$) the EDS spectrum and XRD pattern e) of the rod-shaped FeOOH mesostructures and the c) TEM and d) dark-field images of a corresponding single particle. f) HR-TEM image and f$_1$) FFT pattern of a [001]-oriented rod-shaped FeOOH mesostructure. f$_2$) is an enlarged image from the red square.

Notably, the width of the FeOOH NRs approached 41.60 nm at 2 h. These results let us reasonably envision the generation of FeOOH NRs as a template at the early stage for the subsequent hydrothermal reaction-induced growth of lateral and longitudinal directions of FeOOH crystals.

The fresh FeCl$_2$ solution was colorless; over time, it became red-brown in color, which is consistent with the color of Fe(III), and obvious precipitates appeared on the bottom with increasing incubation time. The particles were collected after 20 days of aging in the FeCl$_2$ stock solution. This material is

consisted of a mixture of γ-FeOOH and α-FeOOH phases with broad peaks in the XRD pattern (Figure S2, Supporting Information). These particles had $\approx$7 nm grain sizes according to the Scherrer equation. The corresponding TEM image indicates the existence of many small nanoparticles. With further aging of the FeCl$_2$ solution, reflection peaks displayed sharper full-width at half-maximum values, suggesting the generation of larger α-FeOOH crystals. Meanwhile, there was a decrease in the relative intensity of the γ-FeOOH crystal structure. The TEM image (Figure S3, Supporting Information) and Table S2 in the Supporting Information show a trend of gradual anisotropic growth of FeOOH crystals, resulting in rod lengths from $\approx$56 nm (30 days) to 175 nm (350 days). Indeed, the yield of precipitates increased up to 67% after 39 days from $\approx$12% at 20 days. The yield reached a plateau ($\approx$80%) between 42 days and 295 days (Figure S4, Supporting Information) in accordance with the inductively coupled plasma atomic emission spectroscopy measurement, showing the preferred growth of orthorhombic α-FeOOH crystals as a more stable phase in this Cl$^-$ ion-based aqueous environment.[30] Through visual observation, TEM,

XRD, and inductively coupled plasma mass spectrometry analyses, we concluded the precipitation of the primary FeOOH particles in the FeCl$_2$ stock solution with respect to aging time. The possible reaction formula could be represented as[26]

$$2Fe^{2+} + 3H_2O + \frac{1}{2}O_2 \rightarrow 2FeOOH + 4H^+ \tag{1}$$

Indeed, the pH value of the Fe mother solution decreased from 4.3 to 2 after the aging process (Figure S5, Supporting Information), suggesting the release of protons from reaction (1). We speculate that the production of FeOOH nanocrystals occurs after the simultaneous oxidation and precipitation (i.e., the hydrolysis-condensation process) reactions[31] during the aging process in the FeCl$_2$ solution.

Based on an insight regarding the secondary growth process, we demonstrated the preparation of the FeOOH mesostructures with different aspect ratios by aging the FeCl$_2$ stock solution for the appropriate time. **Figure 2** shows the TEM results of the shape-controlled synthesis of sophisticated
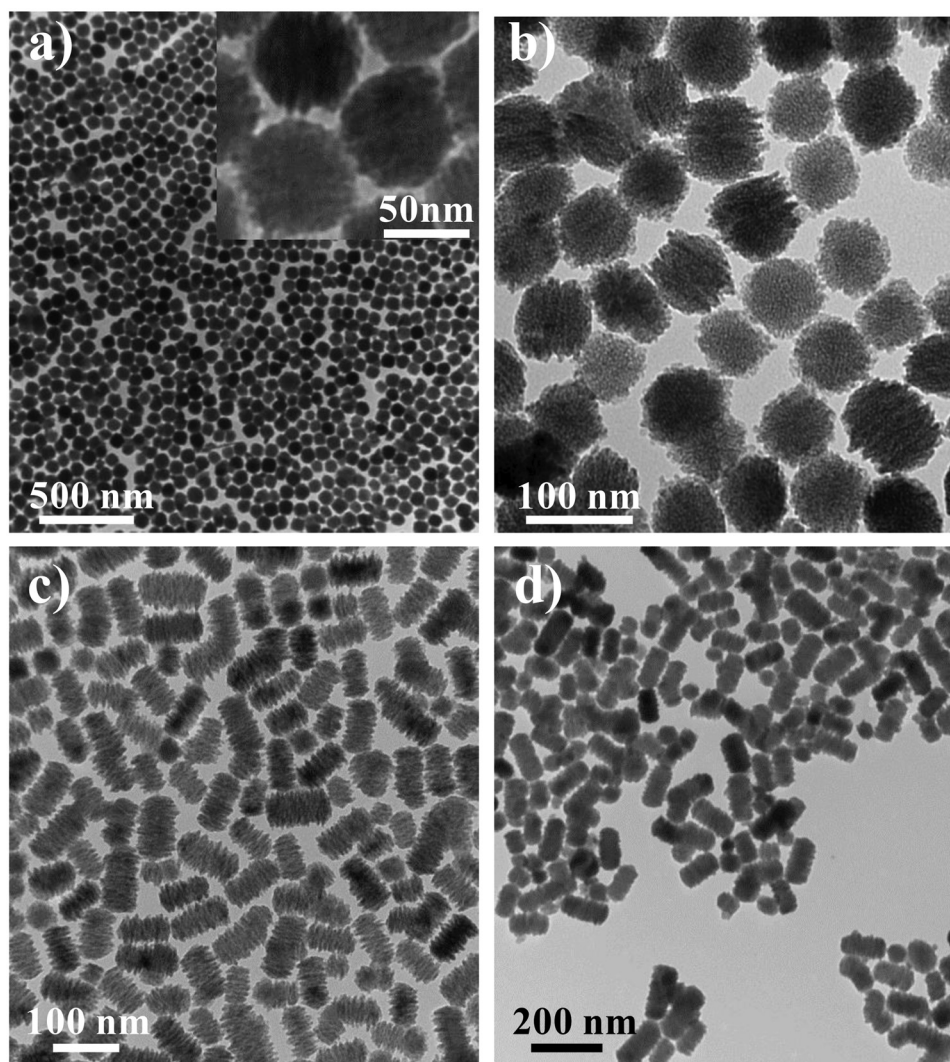

Figure 2. TEM images of as-synthesized FeOOH mesostructures obtained using an FeCl$_2$ solution after aging for a) 8, b) 14, c) 30, and d) 64 days.

ADVANCED
SCIENCE NEWS

www.advancedsciencenews.com

NANO · MICRO
small

www.small-journal.com

FeOOH mesostructures. Spherical FeOOH mesostructures (aspect ratio of ≈1) were obtained using an $FeCl_2$ solution aged for 8–14 days. This isotropic growth of FeOOH nanoparticles could be attributed to the absence of the initial precipitates with rod shapes. Extending the aging time of the $FeCl_2$ solution to 30–110 days resulted in the production of FeOOH NRs with different dimensions, but retaining aspect ratios between 2.08 and 2.23 (see Figure 2 and Figure S6 and Table S1, Supporting Information). The aspect ratio of the FeOOH NR particle dramatically increased to 4.64 based on the perfect growth along the long-axis of the initial precipitates in the $FeCl_2$ stock solution aged for 310 days (Figure S6, Supporting Information).

When all the above results are taken into consideration, it is reasonable that the initially formed α-FeOOH precipitates acted as primary particles, which played the role of a self-template for subsequent secondary growth. The size and aspect ratios of the as-synthesized α-FeOOH mesostructures were controllable using the desired primary α-FeOOH particles from the $FeCl_2$ stock solution after different aging times. Notably, the TEM image (Figure S3, Supporting Information) and Table S1 in the Supporting Information show the irregularly shaped particles and γ-FeOOH materials (smaller particles) at 39 days, which were not present in the final product (Figure 1a,b). We propose that the Ostwald ripening mechanism[25] assisted in dissolving the small and/or high surface energy particles for a subsequent re-precipitation of the α-FeOOH species at the surface of the primary α-FeOOH NRs. Size focusing was observed for the later growth of the α-FeOOH mesostructure in comparison with the corresponding primary α-FeOOH materials. To clarify the growth mechanism of mesostructures, we then investigated the surface characteristics before and after the hydrothermal reaction by using an $FeCl_2$ stock solution aged for 350 days as the starting material. These nanoparticles were subjected to Fourier transform-infrared spectroscopy (FT-IR) measurements (Figure S7, Supporting Information). No vibration signals were observed between 500 and 4000 cm^{-1} for the FeOOH precipitates, indicating the absence of organic molecules at the surface of the particles. The surface to which carboxyl groups attached was demonstrated by FT-IR spectra, in which vs(COO-) and vas(COO-) groups with bridging major bidentate and minor unidentate coordination adhered to the particles.[13] A weight loss of ≈3.5% for the carboxylate capping molecules was determined on the basis of thermogravimetric analysis (Figure S8, Supporting Information). A comparative ligand-free experiment without TMA/citrate reagents (Figure S9, Supporting Information) resulted in the generation of larger and polyhedron Fe_2O_3 crystals by using the $FeCl_2$ stock solution aged for 350 days as an example. Porous FeOOH NRs were not obtained in this ligand-free synthesis. We found that substituting citrate with either malic acid or 2-ketoglutaric acid did not result in creating the mesostructures of the FeOOH NRs (Figure S10, Supporting Information). It could be speculated that the residual iron species in the $FeCl_2$ stock solution bonded with tri-carboxylate TMA/citrate ligands, leading to the formation of stable ligand–iron complexes. These complexes not only assist the self-assembly process of secondary FeOOH species and primary FeOOH NRs through a number of carboxylate bridges, but also limit the fast phase transformation from FeOOH to Fe_2O_3. Defects (labeled D) and lattice misorientations (labeled M) were observed in the enlarged image of selected regions (within the red square of Figure 1f), possibly due to the incorrect structural arrangement in the process of orientation attachment.[32]

Rod-like iron oxide mesostructures have presented high affinity for cell surface receptors and passive accumulation in tissues through polyvalent binding.[33] Therefore, in the process of bioimaging, the toxicity issue must be addressed prior to the application of α-FeOOH rod-like mesostructures in cells or tissues. Analyzed by the MTT assay (MTT = 3-(4,5-dimethylthiazol-2-yl)-2,5-diphenyltetrazolium bromide), the α-FeOOH rod-like mesostructure (39 days) showed low cytotoxicity to human A549 epithelial cells over 1–3 days of incubation. (**Figure 3**a). The addition of α-FeOOH rod-like mesostructures did not cause severe interference for the spectrophotometric analysis of MTT (Figure S11, Supporting Information). Although α-FeOOH rod-like mesostructures (100 ppm) did not affect the proliferation of cells (Figures S12 and S13, Supporting Information), we also checked the potential cell destruction of the cellular plasma membrane by measuring lactate dehydrogenase[34] (LDH) leakage (Figure 3b). One can see that 0–50 $ppm_{[Fe]}$ of α-FeOOH rod-like mesostructures did not cause LDH leakage after 24 h of exposure. Only ≈17% of LDH leakage was detectable when the treatment concentration reached 100 $ppm_{[Fe]}$, while a gradual decrease of LDH activity is observed from 500 $ppm_{[Fe]}$ to 3000 $ppm_{[Fe]}$. Furthermore, the hemolysis experiment (Figure 3c,d) presented a rate of less than 2.5% even at the highest concentration of 3000 $ppm_{[Fe]}$. No membrane destruction of red blood cells (RBCs) occurred after treating the α-FeOOH rod-like mesostructures. Overall, our toxicity examination with different biomolecular assays demonstrated that α-FeOOH rod-like mesostructures do much less harm to human epithelial cells and RBCs compared with other THG contrast agents, such as toxic Ag nanoparticles,[35] lipid-enclosed CdSe,[36,37] and oxygen-sensitive Si nanomaterials.[21] In addition, we administered 3000 $ppm_{[Fe]}$ to five groups of male BALB/c mice (weight range: 18–25 g). There was no acute toxicological impact on the mice and no significant change in body weight at 2 weeks postinjection (Figure S14, Supporting Information).

Next, we examined the contrast capability of α-FeOOH rod-like mesostructures (39 days) for potential multiphoton imaging and microscopy. The multiphoton excitation at the second near infrared (NIR II) window (1–1.4 μm) can greatly reduce the scattering attenuation and pigment absorption in biological tissues, thus achieving deep tissue in vivo imaging.[23,24] The commonly adopted imaging modalities include two-photon fluorescence (TPF), second-harmonic generation (SHG), and THG. For particles without fluorescence properties, the SHG and THG contrasts can be exploited. The contrasts are coherently generated and integrated within the focal volume of the laser. For nanoparticles with sizes well below the coherence length of the THG process,[19] the signal yields are proportional to the square of the nonlinear dipole moment, thus the square of the particle volume. For FeOOH rods, the refractive indices at 410 and 1230 nm are roughly 2.32 and 1.8, respectively. The wave vector mismatch between THG waves and fundamental excitation waves result in an estimated coherence length of 394 nm, which is well above the dimension of our FeOOH mesostructures. To calibrate the total solid volume effects on the yields of multiphoton contrast, we equalized the volume
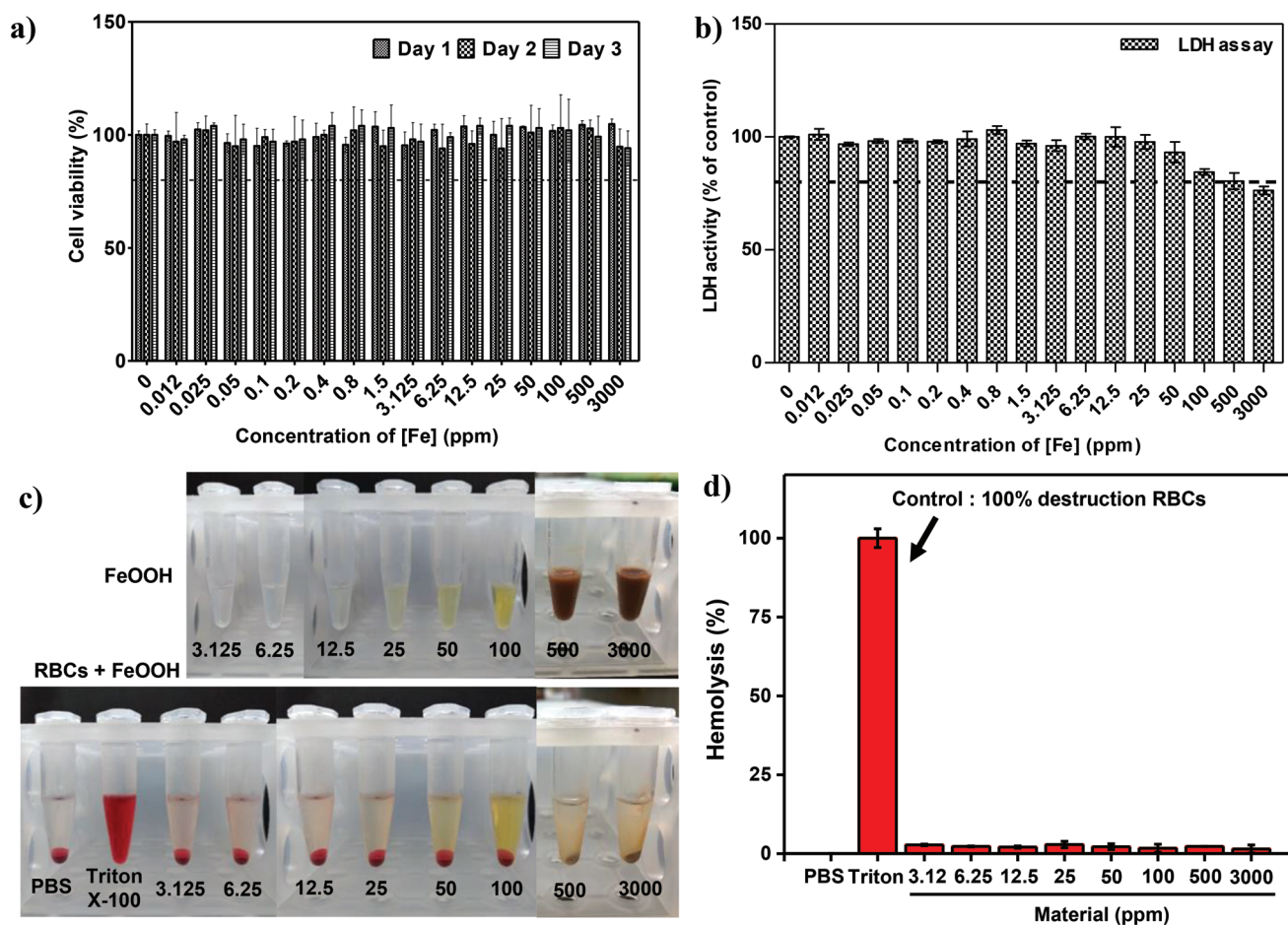
ADVANCED
SCIENCE NEWS
www.advancedsciencenews.com

NANO · MICRO
small
www.small-journal.com

Figure 3. The viability of the A549 lung cancer cells after being treated with different concentrations of α-FeOOH rod-like mesostructures (0–3000 ppm$_{[Fe]}$) for a) 24, 48, and 72 h with the MTT assay and b) for 24 h with the LDH assay. Error bars represent the standard error of four replicates. c) The colors of the α-FeOOH rod-like mesostructures at different concentrations (up) represent the background solution with a yellow color and the hemolysis assay of the negative control (PBS), and the positive control (Triton X-100). α-FeOOH rod-like mesostructures (3.125–3000 ppm$_{[Fe]}$) incubated with the RBCs (bottom). d) Relative rate of hemolysis in human RBCs upon incubation with α-FeOOH rod-like mesostructure suspension at incremental concentrations after subtracting the corresponding absorbance in the background solution.

concentration of the Fe-O/OH composite according to the atomic absorption measurement (see Figure S26, Supporting Information, and the corresponding caption). By dropping the same volume of solution on the surface of a glass slide, we analyzed whether there was extra enhancement of the SHG or THG signal other than the total solid volume effects. We used a 1230 nm femtosecond Cr:forsterite laser to perform multiphoton spectroscopy and imaging on α-FeOOH rod-like mesostructures (Figure S15, Supporting Information). Compared with bare α-FeOOH NRs (39 days), we found an 11-fold enhancement in THG signals for rods with mesostructures (**Figure 4**a). No significant TPF signals could be measured. One possible reason for the enhanced THG yield might be the increased absorption at the third harmonic wavelength (see Figure S16, Supporting Information).[35,38] This prominent absorption of the electronic state might be due to the formation of strong Fe-O/OH bonds. Evidence on the XRD measurements showed that α-FeOOH rod-like mesostructures have narrower reflection peaks (Figure S2, Supporting Information) than those of bare α-FeOOH NRs (39 days, without a hydrothermal

reaction), indicating a better crystallization level and stronger bonds. The efficient dipolar transition from O^{2-} 2p to Fe^{3+} 3d thus resonantly enhanced the third-order susceptibility in the high crystallization[39–41] of α-FeOOH rod-like mesostructures (39 days).

After incubation of A549 lung cancer cells with α-FeOOH rod-like mesostructures for 24 h, the cells were washed with phosphate-buffered saline (PBS) three times to remove nanocrystals outside the cells. In the bright-field images, the distribution of α-FeOOH rod-like mesostructures can be clearly identified inside the cells (Figure 4b) as brown granules. In THG microscopy, intracellular granules exhibit strong THG signals and the cellular profiles are clearly revealed (Figure 4c). En face and cross-sectional analyses of high-resolution multiphoton images (Figures S17 and S18, Supporting Information) clearly revealed that α-FeOOH rod-like mesostructures (magenta color in Figure 4d and Figure S18, Supporting Information) were readily internalized and sequestered in organelles outside the nuclei (cyan color in Figure 4d and Figure S18, Supporting Information) of A549 cells. The location of cells
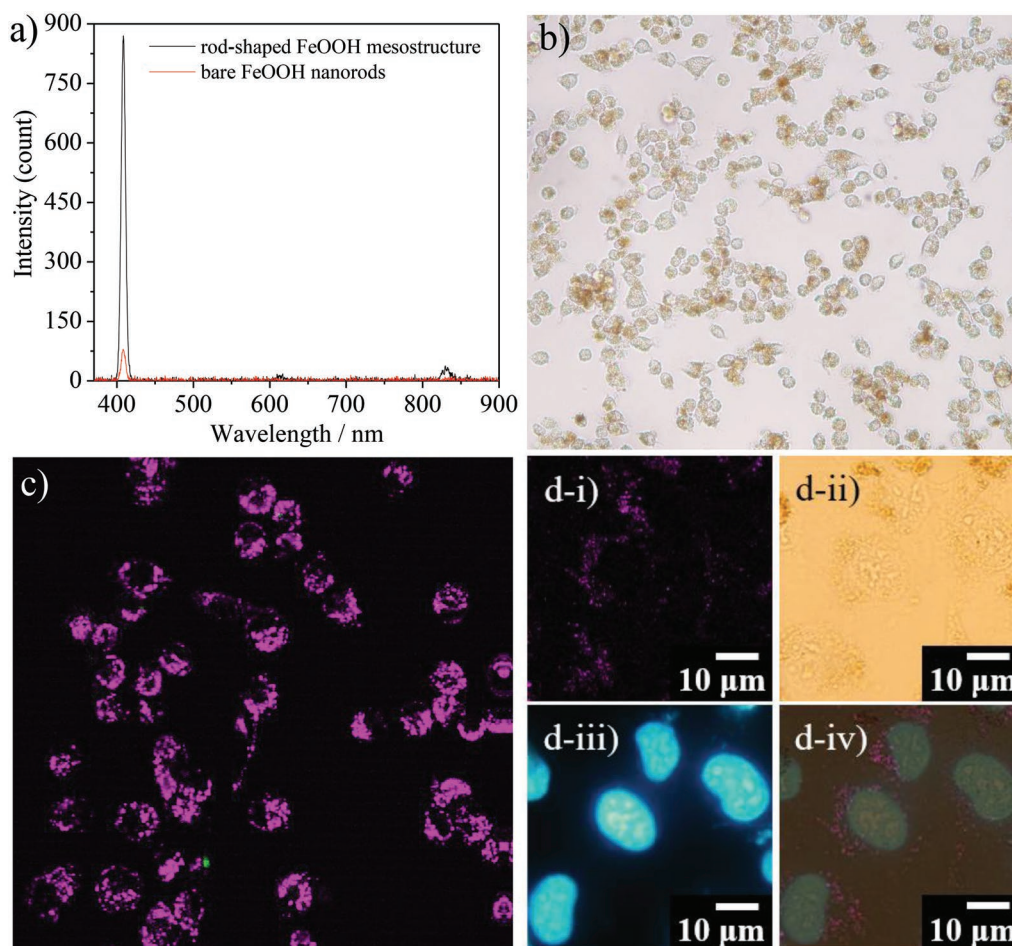
ADVANCED
SCIENCE NEWS
www.advancedsciencenews.com

NANO · MICRO
small
www.small-journal.com

Figure 4. a) Nonlinear optical spectra of the α-FeOOH rod-like mesostructures and bare FeOOH NRs with femtosecond laser excitation at 1230 nm. b) bright field image and c) THG microscopy image of human lung cancer cells (A549) treated with α-FeOOH rod-like mesostructures. d) Series of enlarged images of human lung cancer cells (A549) treated with 0.2 mL of α-FeOOH rod-like mesostructures (500 ppm$_{[Fe]}$) and a counterstain for nuclei with DAPI i) THG microscopy image, ii) bright field image, iii) fluorescent image of DAPI, and iv) merged image from (i) to (iii). Fields of view: c) 240 μm × 240 μm; and d) 60 μm × 60 μm.

was characterized by the bright-field images, two-photon fluorescence of 4′,6-diamidino-2-phenylindole (DAPI) excited at 716 nm (cyan color in Figure S18, Supporting Information), and two-photon auto-fluorescence of cell porphyrins (600–700 nm) excited at 800 nm (yellow color in Figure S18, Supporting Information). Without treatment with the α-FeOOH rod-like mesostructures, the THG contrast of granules in A549 cells alone was much weaker (Figure S17a, Supporting Information). By analyzing the mean THG intensity of the cells, we found that α-FeOOH rod-like mesostructures maintained a strong THG contrast to reveal the cell morphology over 3 days (Figure S17b, Supporting Information). This nonbleaching and strong THG signals make it a reliable contrast agent suitable for long-term cell imaging or for the study of particle metabolism by cells.

Then we prepared α-FeOOH@DA rod-like mesostructures followed by conjugating lectin[42] on the particle surface (Figure S19, Supporting Information) for the first demonstration of THG angiography in vivo, where dopamine (DA) supplied an amine group to interact with the amine end at the lectin molecule with HOOC-PEG-COOH as a

linker via the N-(3-dimethylaminopropyl)-N′-ethylcarbodiimide hydrochloride/N-hydroxysuccinimide (EDC/NHS) coupling reaction (see the Experimental Section in the Supporting Information). The surface functionalization of lectin can improve the binding affinity of α-FeOOH@DA rod-like mesostructures to the glycocalyx layers on the endothelial cells of vessel walls.[27] Compared with typical histology images of mouse ears,[43] THG microscopy can noninvasively resolve the sebaceous glands, vessels, and other organelles in vivo in normal tissues (**Figure 5**a).[44,45] On the other hand, SHG microscopy can reveal the collagen networks (Figure 5b), where the THG signals are relatively weak. Although THG imaging can reveal the capillaries through the contrast of RBCs, the vessel walls cannot be outlined well in large vessels (Figure S20a, Supporting Information). After intravenous injection of α-FeOOH@DA-Lectin rod-like mesostructures, the strong and dot-like THG signals flowed in the vessels immediately (Figures S20b and S21a, Supporting Information), and the circulation was maintained for more than 16.2 min. Meanwhile, the mesostructures gradually deposited on the blood vessel walls, giving strong THG
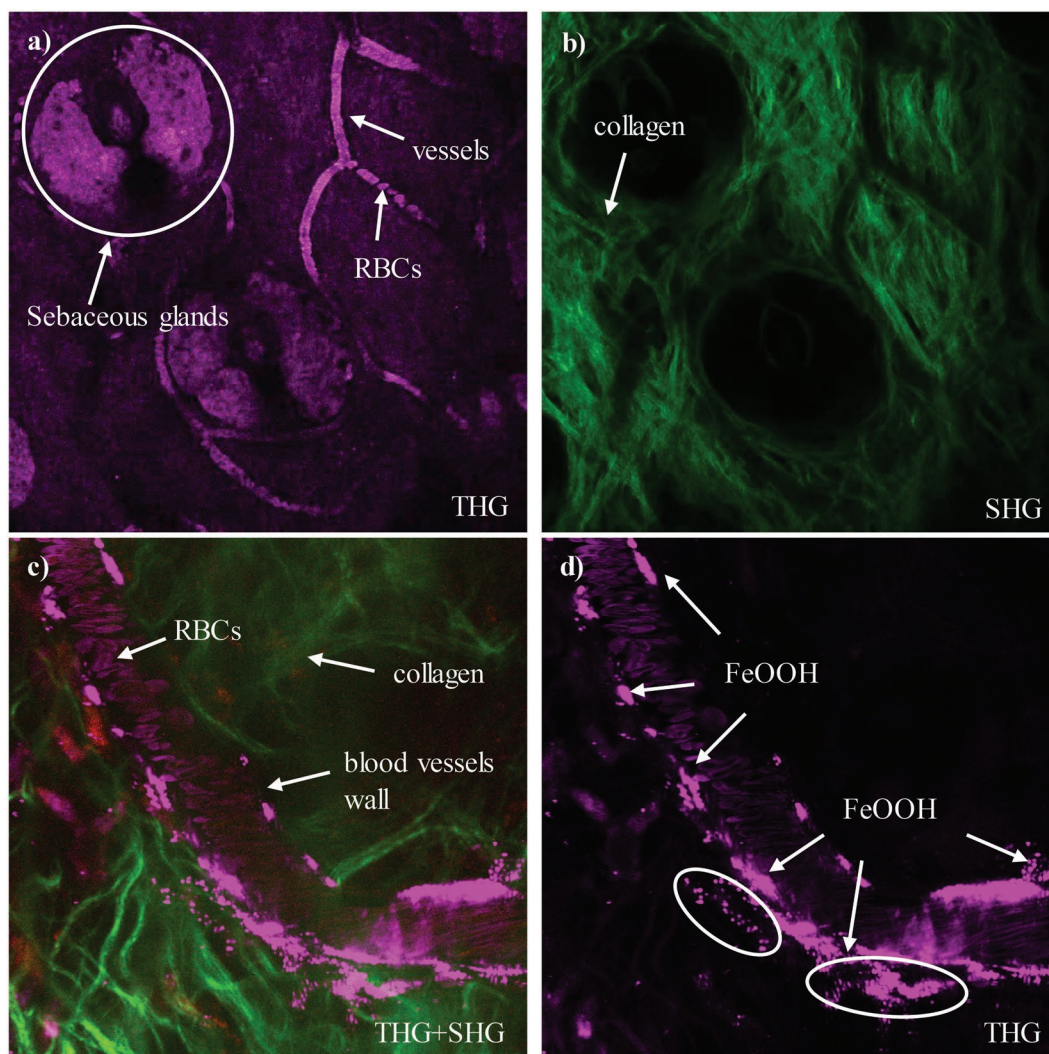
**ADVANCED
SCIENCE NEWS**
www.advancedsciencenews.com

NANO · MICRO
small
www.small-journal.com

Figure 5. a) THG (magenta color) and b) SHG (green color) images of a mouse ear in vivo. In vivo c) THG+SHG and d) THG images of the normal mouse ear after the intravenous injection of 0.1 mL FeOOH@DA-Lectin mesostructures (3000 ppm$_{[Fe]}$). THG image in d) shows deposition on the blood vessel wall (indicated by white arrows) and some of the FeOOH@DA-Lectin particles leaked into the tissue, as highlighted by white circles. Fields of view: a,b) 240 µm × 240 µm; c,d) 80 µm × 80 µm.

contrast (Figure S20c,d, Supporting Information). Figure S21b in the Supporting Information shows that the THG signals on blood vessel walls were gradually increased and reached a plateau after 20 min (see movie S1, Supporting Information). In another view at 30 min postinjection (Figure 5c,d), we clearly observed the characteristic disk-shaped RBCs from the THG image, which is very different from the dot-like contrast of the FeOOH@DA-Lectin mesostructure around the blood vessel walls. Blood cells still flowed through the vessels after 30 min, so we confirmed that the FeOOH@DA-Lectin mesostructures did not cause thrombus in circulation. Some of the particles were leaked from the vessels into the collagen networks with strong SHG signals (Figure 5c), possibly resulting from the scavenging uptake of macrophages (highlighted by white circles in Figure 5d). It is worth noting that all THG signals of FeOOH@DA-Lectin mesostructures were obviously stronger than those of RBCs in vessels. Therefore, we can easily identify the flush-in of FeOOH@DA-Lectin particles in circulation

from the time-course THG imaging after injection. The distribution of deposited FeOOH@DA-Lectin nanoparticles delineated the outline of vessel walls. These results demonstrated the first THG angiography in vivo, which is a valuable function for image studies of tumor angiogenesis,[42,46] biosensors,[47] and nanomedicine pharmacokinetics.

Furthermore, we prepared FeOOH@DA mesostructure-conjugated QDs (QD$_{655}$) and lectin (Figure S22, Supporting Information) to confirm the particle distributions in vivo. The corresponding synthesis method was included in the Experimental Section in the Supporting Information. To observe the two-photon red fluorescence of QD, we used a 635 nm long-pass filter (Figure S23, Supporting Information) to block the 615 nm SHG signals from collagens. After intravenous injection of the FeOOH@DA-QD-Lectin mesostructures, the TPF signals of QD were only found in the vessels (green color, Figure S24a, Supporting Information) and co-localized with the strong THG signals of α-FeOOH mesostructures (Figure S24b, Supporting

**ADVANCED
SCIENCE NEWS**
www.advancedsciencenews.com

NANO · MICRO
small
www.small-journal.com

Information) even at 2 min postinjection. The resulting white color in the merged image of Figure S24c in the Supporting Information validates the presence of the injected FeOOH@DA-QD-Lectin nanoagents, which were not quickly cleared by the reticulo-endothelial system and were retained in circulation for a while. This result depicts the possible integration of α-FeOOH rod-like mesostructures to other fluorophores as promising biomedical probes to monitor the release of fluorophore drugs from mesostructured α-FeOOH nanocarriers in vivo.

3. Conclusion

In conclusion, our demonstration showed a new chemical synthesis strategy for the integration of a common aging process with a ligand-assisted Ostwald ripening reaction to produce shape-controlled α-FeOOH nanocrystals with mesostructures. Nonlinear optical studies of α-FeOOH rod-like mesostructures showed strong and structure-enhanced THG signals excited by an infrared femtosecond laser. This intrinsic contrast allows FeOOH meso-nanorods to be observed by THG microscopy in cellular imaging. When intravenously applied, FeOOH@DA mesostructures conjugated with lectin showed a long retention time of 16.2 min in circulation, and they outlined the blood vessel walls after affinity deposition. The distribution of the mesostructures after intravenous injection can thus be evaluated in vivo. In the future, we could test coating of different lectins at different injection concentration to avoid aggregation and achieve even deposition of mesostructures on the vessel walls. Our results open new avenues for future applications of FeOOH NRs in cell tracking, angiography, and diagnostic photomedicine.

4. Experimental Section

Materials: Iron(II) chloride tetrahydrate (FeCl$_2$·4H$_2$O, 99–102%; Merck), trisodium citrate (100%; J. T. Baker), benzene-1,3,5-tricarboxylic acid (TMA, 98%; Alfa Aesar), lectin (unconjugated wheat germ agglutinin, determined homogenous by sodium dodecyl sulfate polyacrylamide gel electrophoresis; Vector Laboratories), NHS-PEG-COOH (MW = 1000 Da, 95%; Huateng Pharma), HOOC-PEG-COOH (MW = 662.7 Da, ≥95%; JenKem Technology), dopamine hydrochloride (≥98%; Sigma-Aldrich), EDC (≥98%; Sigma-Aldrich), NHS (98+%; Alfa Aesar), and QD$_{655}$ (Qdot655 ITK amino (PEG) QDs, 2 n moles in 50×10^{-3} M borate; Life Technologies) were purchased for use without purification.

Preparation of α-FeOOH Rod-Like Mesostructures: α-FeOOH rod-like mesostructures were prepared by a one-pot hydrothermal reaction that was well-developed for sub-gram level preparations. Briefly, FeCl$_2$·4H$_2$O (10 mL, 50×10^{-3} M), TMA (4.5 mL, 25×10^{-3} M), NaOH (18 mg), and trisodium citrate (0.15 g) were mixed by stirring and then immediately transferred to a 23 mL Teflon-lined stainless steel autoclave to be heated at 200 °C for 12 h. A repeated centrifugation/washing process with deionized water was employed to purify the as-synthesized products. After purification, the as-prepared α-FeOOH rod-like mesostructures were subjected to various analyses or stored at 4 °C for further use.

Preparation of FeOOH@DA-Lectin Mesostructures: First, 2 mL of α-FeOOH rod-like mesostructures (500 ppm$_{[Fe]}$) was incubated with 2 mL of DA solution (0.2 mg mL^{-1}) under vigorous stirring for 2 h. The resulting α-FeOOH@DA mesostructure product was collected and purified by a repeated centrifugation and redispersion process with water more than three times. Subsequently, lectins were reacted with

the NHS-end group of NHS-PEG-COOH (0.05 mg mL^{-1} in desiccative dimethyl sulfoxide) at a 2:1 molar ratio in 10×10^{-3} M HEPES buffer (10×10^{-3} M, N-(2-hydroxyethyl)piperazine-N'-2-ethanesulfonic acid, 137×10^{-3} M NaCl, pH 7.5, sterilized) overnight. Then, the lectins-PEG-COOH was incubated with 1.5 mg mL^{-1} EDC and a 1.5 mg mL^{-1} NHS solution for 2 min and then reacted with the FeOOH@DA mesostructure solution at 4 °C for 1 h. A repeated centrifugation and redispersion process with a PBS solution was implemented to purify the FeOOH@DA-Lectin mesostructures.

Preparation of FeOOH@DA-QD-Lectin Mesostructures: To prepare FeOOH@DA-QD-Lectin mesostructure, 0.2 mL of amino QD$_{655}$ (2 p moles) was reacted with 1 mL of FeOOH@DA mesostructures (500 pp$_{[Fe]}$) in the presence of 1 mL HOOC-PEG-COOH (1 mg mL^{-1}), 1.5 mg mL^{-1} EDC, and 1.5 mg mL^{-1} NHS to form FeOOH@DA@QD nanohybrid. After 1 h of reaction time at 4 °C, the sample was collected by repeating the centrifugation and redispersion (with a PBS solution) process. Next, the lectins-PEG-COOH molecule was freshly prepared before bioconjugation. The immobilization of the COOH groups of the lectins-PEG-COOH onto the amino groups of 1 mL FeOOH@DA@QD mesostructures (500 pp$_{[Fe]}$) was performed via an EDC/sulfo-NHS ester surface reaction, which was performed via the same process as the above bioconjugation experiment.

Cell Study: The cells used in the labeling observations were human lung cancer cells (A549). Cells were incubated in RPMI1640 culture medium in a glass bottom petri dish and incubated at 37 °C under 5% CO$_2$. The 8000 cells were cultured with 0.2 mL of 500 ppm$_{[Fe]}$ FeOOH mesostructure solution overnight. To keep the cells in their normal physiological status, the solvent of FeOOH rod-like mesostructures was first replaced by the culture medium instead of adding it to the dish directly. The FeOOH solution in the Eppendorf tube was centrifuged at the very beginning. Then, the supernatant solution was removed and replaced with RPMI1640 culture medium to the same volume, and then pipetted several times. These washing processes were performed three times to ensure that the solution was suitable for cell growth.

In Vitro Nonlinear Spectroscopy and Microscopy System: The laser was a home-built Cr:forserite femtosecond laser operating at 1230 nm with a 100 fs pulsewidth, 110 MHz pulse repetition rate, and an average output power of approximately 500 mW. The average power for the spectroscopy experiment was approximately 60 mW after the 60×0.9 NA objective (Olympus). The corresponding peak intensity at the focus was roughly 1×10^{12} W cm^{-2}. For THG microscopy, the average power excited on the sample was approximately 30 mW after a 60×1.2 NA objective (Olympus). The corresponding peak intensity at the focus was roughly 8.88×10^{11} W cm^{-2}. During the imaging experiment, the petri-dish was placed in a homemade micro-incubator, which provided a 37 °C and 5% CO$_2$ environment. The objective was warmed up as well by an objective heating ring. During illumination, the third harmonic was generated and the two-photon fluorescence was emitted simultaneously; the two signals were split by a 490 nm short pass dichroic beam splitter, filtered by a 410 nm bandpass filter and 650 nm long pass filter, respectively, and then acquired by two photomultiplers (PMTs). The 410 nm bandpass filter had a 10 nm bandwidth to block three-photon luminescence at a wavelength longer than 420 nm. The acquired images had 512×512 pixels with fields of view of 250 μm × 250 μm.

In Vivo Nonlinear Microscopy System: The Nikon Ti2 A1R MP+ multiphoton system was used to observe FeOOH@DA-Lectin mesostructures in vessels by tail vein injection. The available excitation wavelength was tuned from 700 to 1300 nm. At 1250 nm excitation, the THG and SHG images were collected by nondescanned detectors. Images were acquired sequentially using a $40 \times$ NA 1.15 (Nikon, CFI Apochromat LWD Lambda S 40XC WI) water immersion objective. The peak intensity after the objective was the same as that of in vitro imaging. The bandpass filter (415–485 nm) was also put before the PMT to select the THG signals. In the dermis layer of normal mouse ear samples (Figure S25a, Supporting Information), the typical multiphoton spectrum excited at 1250 nm was dominated by SHG (Figure S25b,

Supporting Information) and only THG signals were found within the spectral range of the bandpass filter (Figure S25c, Supporting Information). Therefore, it was verified that the blue (415–485 nm) channel primarily revealed the contrast of THG. The sebaceous glands, blood cells, and lipids were typical biological objects that were label-free observed in in vivo THG microscopy (Figure S25a, Supporting Information). For THG angiography, BALB/c mice were injected with 100 µL of 3000 ppm$_{[Fe]}$ α-FeOOH@DA-Lectin rod-like mesostructures or α-FeOOH@DA-QD-Lectin rod-like mesostructures via tail-vein catheterization, and the images were captured and recorded for 30 min after injection. After observation, the mice survived without any adverse effects.

Animal Model and Anesthesia: The protocols of the animal experiments were approved by the Animal Ethics of Macau University (UMARE-030-2016). The α-FeOOH rod-like mesostructures were suspended in PBS and injected into 4 week old male BALB/C mice with 3000 ppm$_{[Fe]}$ in a volume of 100 µL, and the mice were purchased from the Animal Center of Macau University. All of the mouse body weights were approximately 18–25 g at the beginning of the experiment, and the mice were sacrificed after 28 days of experimental observation postinjection. Isoflurane vaporized at concentrations of 0.8–1.5% was used under anesthesia in the experiment for its effectiveness, lack of side effects, and rapid washout in continuous time-course imaging and prolonged experimental observations. The body temperature was concurrently maintained at 37 °C with a warming pad (RightTemp, Kent Scientific) during the entire period the mice were under anesthesia until recovery.

Supporting Information

Supporting Information is available from the Wiley Online Library or from the author.

Conflict of Interest

The authors declare no conflict of interest.

[1] J. Torrent, V. Barrón, in *Encyclopedia of Surface and Colloid Science* (Ed: A. T. Hubbard), Marcel Dekker, Inc., New York **2002**, p. 1438.
[2] J. Zhang, J. Zheng, *Anal. Methods* **2015**, *7*, 1788.
[3] X. Wang, X. Chen, L. Gao, H. Zheng, M. Ji, C. Tang, T. Shen, Z. Zhan, *J. Mater. Chem.* **2004**, *14*, 905.
[4] Y. Wang, J. Cao, S. Wang, X. Guo, J. Zhang, H. Xia, S. Zhang, S. Wu, *J. Phys. Chem. C* **2008**, *112*, 17804.
[5] A. K. Patra, D. Kim, *ACS Sustainable Chem. Eng.* **2017**, *5*, 1272.
[6] I. Andjelkovic, D. N. H. Tran, S. Kabiri, S. Azari, M. Markovic, D. Losic, *ACS Appl. Mater. Interfaces* **2015**, *7*, 9758.
[7] L. A. Wijenayaka, G. Rubasinghege, J. Baltrusaitis, V. H. Grassian, *J. Phys. Chem. C* **2012**, *116*, 12566.
[8] R. Chalasani, S. Vasudevan, *J. Phys. Chem. C* **2011**, *115*, 18088.
[9] J. H. Hsu, C. R. Chang, P. C. Kuo, J. H. Huang, *J. Magn. Magn. Mater.* **1990**, *89*, 167.
[10] T. M. Liu, J. Conde, T. Lipiński, A. Bednarkiewicz, C. C. Huang, *Prog. Mater. Sci.* **2017**, *88*, 89.
[11] T. M. Liu, J. Conde, T. Lipiński, A. Bednarkiewicz, C. C. Huang, *NPG Asia Mater.* **2016**, *8*, e295.
[12] C. C. Huang, P. Y. Chang, C. L. Liu, J. P. Xu, S. P. Wu, W. C. Kuo, *Nanoscale* **2015**, *7*, 12689.
[13] M. Y. Liao, P. S. Lai, H. P. Yu, H. P. Lin, C. C. Huang, *Chem. Commun.* **2012**, *48*, 5319.
[14] H. Chen, J. Burnett, F. Zhang, J. Zhang, H. Paholak, D. Sun, *J. Mater. Chem. B* **2014**, *2*, 757.
[15] M. Chu, Y. Shao, J. Peng, X. Dai, H. Li, Q. Wu, D. Shi, *Biomaterials* **2013**, *34*, 4078.
[16] M. Y. Liao, C. H. Wu, P. S. Lai, J. Yu, H. P. Lin, T. M. Liu, C. C. Huang, *Adv. Funct. Mater.* **2013**, *23*, 2044.
[17] T. J. Li, C. M. Chang, P. Y. Chang, Y. C. Chuang, C. C. Huang, W. C. Su, D. B. Shieh, *NPG Asia Mater.* **2016**, *8*, e277.
[18] J. Zhang, J. Li, S. Chen, N. Kawazoe, G. Chen, *J. Mater. Chem. B* **2016**, *4*, 5664.
[19] H. Maeda, Y. Maeda, *Langmuir* **2011**, *27*, 2895.
[20] R. W. Boyd, *Nonlinear Optics*, 3rd ed., Academic Press, San Diego, CA **2008**.
[21] Y. Jung, L. Tong, A. Tanaudommongkon, J. X. Cheng, C. Yang, *Nano Lett.* **2009**, *9*, 2440.
[22] N. Chen, Y. He, Y. Su, X. Li, Q. Huang, H. Wang, X. Zhang, R. Tai, C. Fan, *Biomaterials* **2012**, *33*, 1238.
[23] L. A. Sordillo, Y. Pu, S. Pratavieira, Y. Budansky, R. R. Alfano, *J. Biomed. Opt.* **2014**, *19*, 056004.
[24] L. Dubreil, I. Leroux, M. Ledevin, C. Schleder, L. Lagalice, C. Lovo, R. Fleurisson, S. Passemard, V. Kilin, S. Gerber-Lemaire, M.-A. Colle, L. Bonacina, K. Rouger, *ACS Nano* **2017**, *11*, 6672.
[25] E. Matijevic, *Chem. Mater.* **1993**, *5*, 412.
[26] N. Singh, B. Manshian, G. J. Jenkins, S. M. Griffiths, P. M. Williams, T. G. Maffeis, C. J. Wright, S. H. Doak, *Biomaterials* **2009**, *30*, 3891.
[27] H. Kataoka, A. Ushiyama, H. Kawakami, Y. Akimoto, S. Matsubara, T. Iijima, *Microsc. Res. Tech.* **2016**, *79*, 31.
[28] S. Reitsma, D. W. Slaaf, H. Vink, M. A. M. J. van Zandvoort, M. G. A. oude Egbrink, *Pfluegers. Arch.-Eur. J. Physiol.* **2007**, *454*, 345.
[29] G. T. Tietjen, S. A. Hosgood, J. DiRito, J. Cui, D. Deep, E. Song, J. R. Kraehling, A. S. Piotrowski-Daspit, N. C. Kirkiles-Smith, R. Al-Lamki, S. Thiru, J. A. Bradley, K. Saeb-Parsy, J. R. Bradley, M. L. Nicholson, W. M. Saltzman, J. S. Pober, *Sci. Transl. Med.* **2017**, *9*, eaam6764.
[30] P. V. Adhyapak, U. P. Mulik, D. P. Amalnerkar, I. S. Mulla, *J. Am. Ceram. Soc.* **2013**, *96*, 731.
[31] R. M. Cornell, U. Schwertmann, *The Iron Oxides: Structure, Properties, Reactions, Occurrences and Uses*, 2nd ed., Wiley-VCH, Weinheim, Germany **2003**.
[32] J. Liu, X. Huang, Y. Li, K. M. Sulieman, X. He, F. Sun, *Cryst. Growth Des.* **2006**, *6*, 1690.

[33] J. H. Park, G. Maltzahn, L. Zhang, M. P. Schwartz, E. Ruoslahti, S. N. Bhatia, M. J. Sailor, *Adv. Mater.* **2008**, *20*, 1630.

[34] H. A. Jeng, J. Swanson, *J. Environ. Sci. Health, Part A: Toxic/Hazard. Subst. Environ. Eng.* **2006**, *41*, 2699.

[35] S. P. Tai, Y. Wu, D. B. Shieh, L. J. Chen, K. J. Lin, C. H. Yu, S. W. Chu, C. H. Chang, X. Y. Shi, Y. C. Wen, K. H. Lin, T. M. Liu, C. K. Sun, *Adv. Mater.* **2007**, *19*, 4520.

[36] C. F. Chang, C. Y. Chen, F. H. Chang, S. P. Tai, C. Y. Chen, C. H. Yu, Y. B. Tseng, T. H. Tsai, I. S. Liu, W. F. Su, C. K. Sun, *Opt. Express* **2008**, *16*, 9534.

[37] C. Y. Lin, T. M. Liu, C. Y. Chen, Y. L. Huang, W. K. Huang, C. K. Sun, F. H. Chang, W. L. Lin, *J. Controlled Release* **2010**, *146*, 291.

[38] T. M. Liu, S. P. Tai, C. H. Yu, Y. C. Wen, S. W. Chu, L. J. Chen, M. R. Prasad, K. J. Lin, C. K. Sun, *Appl. Phys. Lett.* **2006**, *89*, 043122.

[39] M. Zhu, B. Legg, H. Zhang, B. Gilbert, Y. Ren, J. F. Banfield, G. A. Waychunas, *Environ. Sci. Technol.* **2012**, *46*, 8140.

[40] H. Zhang, M. Bayne, S. Fernando, B. Legg, M. Zhu, R. L. Penn, J. F. Banfield, *J. Phys. Chem. C* **2011**, *115*, 17704.

[41] C. Luna, A. D. Cuan-Guerra, E. D. Barriga-Castro, N. O. Núñez, R. Mendoza- Reséndez, *Mater. Res. Bull.* **2016**, *80*, 44.

[42] X. He, F. Liu, L. Liu, T. Duan, H. Zhang, Z. Wang, *Mol. Pharmaceutics* **2014**, *11*, 738.

[43] Q. Lin, A. B. Clark, S. D. McCulloch, T. Yuan, R. T. Bronson, T. A. Kunkel, R. Kucherlapati, *Cancer Res.* **2006**, *66*, 87.

[44] C. H. Yu, S. P. Tai, C. T. Kung, I. J. Wang, H. C. Yu, H. J. Huang, W. J. Lee, Y. F. Chan, C. K. Sun, *Opt. Express* **2007**, *15*, 11167.

[45] C. L. Liu, T. M. Liu, T. Y. Hsieh, H. W. Liu, Y. S. Chen, C. K. Tsai, H. C. Chen, J. W. Lin, R. B. Hsu, T. D. Wang, C. C. Chen, C. K. Sun, P. T. Chou, *Small* **2013**, *9*, 2103.

[46] M. L. S. Silva, *Cancer Lett.* **2018**, *436*, 63.

[47] X. Zhang, Y. Teng, Y. Fu, L. Xu, S. Zhang, B. He, C. Wang, W. Zhang, *Anal. Chem.* **2010**, *82*, 9455.